Synergistic Effects of Surface Chemistry and Topologic Structure from Modified Microarc Oxidation Coatings on Ti Implants for Improving Osseointegration

Rui Zhou,[†] Daqing Wei,*,[†] Jianyun Cao,[†] Wei Feng,[†] Su Cheng,[‡] Qing Du,[†] Baoqiang Li,[†] Yaming Wang,[†] Dechang Jia,[†] and Yu Zhou[†]

[†]Department of Materials Science and Engineering, Harbin Institute of Technology, Harbin, 150080, P. R. China

[‡]Department of Mechanical Engineering, Harbin University of Science and Technology, Harbin, 150001, P. R. China

S Supporting Information

ABSTRACT: Microarc oxidation (MAO) coating containing Ca, P, Si, and Na elements on a titanium (Ti) implant has been steam-hydrothermally treated and further mediated by post-heat treatment to overcome the compromised bone-implant integration. The bone regeneration, bone-implant contact, and biomechanical push-out force of the modified Ti implants are discussed thoroughly in this work. The best *in vivo* performances for the steam-hydrothermally treated one is attributed to the synergistic effects of surface chemistry and topologic structure. Through post-heat treatment, we can decouple the effects of surface chemistry and the nanoscale topologic structure easily. Attributed to the excellent *in vivo* performance of the surface-modified Ti implant, the steam-hydrothermal treatment could be a promising strategy to improve the osseointegration of the MAO coating covered Ti implant.

KEYWORDS: titanium, surface modification, surface chemistry, topologic structure, osseointegration
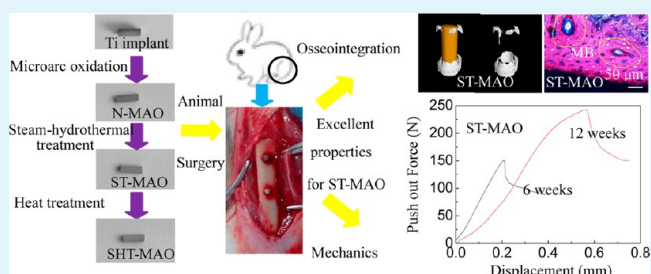
1. INTRODUCTION

The enhanced requirements for metallic implants in dental and orthopedic applications caused by disease or age drive numerous research and development efforts.[1] Titanium (Ti) has been widely accepted as a promising material for metallic implants because of its nontoxicity, high corrosion resistance, and excellent mechanical properties, which satisfactorily meet most of the essential considerations in the design of metallic biomaterials.[2] However, the poor osseointegration of the Ti implant with the surrounding bone tissue limits its application as a load-bearing implant.[3,4] During bone remodeling, previously formed bone is resorbed by osteoclasts to remove microcracks caused by the frequent stress between the Ti implant and bone tissue under load-bearing conditions.[5−7] This directly leads to the osteoporosis of the cortical bone around the Ti implant, which will further result in the failure of the surgery.

On the basis of the mechanism of osseointegration between the implant and surrounding bone tissue (the formation of apatite and growth of collagen fibers),[8] there are two surface-modifying strategies to address the weak osseointegration of the Ti implant: the surface chemistry design and topologic structure design. In the case of surface chemistry design, its effect on the apatite-inducing ability has widely drawn the attention of the researchers.[9−16] The literature on this topic is dominated by studies on the incorporation of active elements and functional groups.[17−21] Such work has indicated that the incorporated elements (Ca, Si, and Na) can affect the apatite nucleation via ion exchange with the simulated body fluid (SBF).[16,22] Similarly, the −OH functional groups (Ti−OH and Si−OH) can effectively improve the apatite-inducing ability of the surface through attracting Ca^{2+} ions for deposition.[19,21] In terms of surface topologic structure design, more and more recent studies have focused on the hierarchical combination of both micro- and nanoscale topologic structure to promote osseointegration on clinically relevant surfaces.[23] The benefits of nanoscale topologic structure are that it plays an important role in osteoblast differentiation and tissue regeneration, attributing to the direct response to the proteins and cell membrane receptors.[24] However, studies have also reported that the effect of nanoscale topologic structure on osteoblast cell proliferation is not stable in the absence of microscale surface structure.[25−27]

Therefore, the surface modification technologies, including microarc oxidation (MAO),[28,29] plasma spraying,[9,10] sol−gel treatment,[11,12] etc. have been used to improve the osseointegration of Ti implants by endowing the implant surface with appropriate surface chemistry and topologic structure. Among the above-mentioned technologies, MAO has attracted great attention because both the microscale porous surface structure

and the chemistry of the as-formed MAO coating can be well adjusted by changing electrolyte composition and electrical parameters.[22,28,30] Though the original formed MAO coating shows poor bioactivity,[31−35] post treatments (in detail, hydrothermal treatment,[17−21] alkali treatment,[36] and chemical treatment[37]) can significantly improve the apatite-inducing ability by introducing the −OH functional groups into the coating. Unfortunately, both the concentration of incorporated elements and mechanical properties of the MAO coating could be dramatically cut by such post treatments.[19,20] Moreover, the surface topologic structure would also be easily changed due to the attacks of corrosive groups.[19,20] As a result, it would further lead to the failure of the surgery owing to the poor interface bonding strength, although the implant surface shows enhanced osseointegration at the early server term.

Our previous work has proved that a relatively new technology, steam-hydrothermal treatment, can improve the apatite-inducing ability of the MAO coating without cutting the incorporated elemental concentration and mechanical properties.[38] Therefore, the original MAO coating covered Ti implant has been steam-hydrothermally treated in this work, which exhibits a distinct hierarchical structural complexity with microscale pores (2−5 μm in diameter) and nanoscale anatase dots and hydroxyapatite (HA) wires. Fortunately, some studies have reported the promising results of increased osseointegration on the hierarchical structural surface,[24] but it is still challenging to create a tailored hierarchical surface without changing the substrate characteristics (particularly the microscale pores and functional group in this work). Interestingly, the post-heat treatment for the hydrothermal-treated sample[39,40] reveals that the as-formed −OH functional group can be easily removed by the heat treatment. Therefore, the previously formed HA nanowires transform to nanopowders after post-heat treatment, which can be easily cleaned by the washing process. Thus, the surface chemistry (as-formed HA) of the steam-hydrothermally treated MAO coating can be further mediated by the post-heat treatment. As a result, we can decouple the effects of surface chemistry and the nanoscale topologic structure easily.

Because there is no report about the synergistic effects of the surface chemistry and topologic structure from steam-hydrothermally treated MAO coating on osseointegration, their influences on the bone regeneration, bone-implant contact, and biomechanical push-out force for the modified Ti implants are discussed thoroughly in this work.

2. MATERIALS AND METHODS

2.1. Fabrication of Ti Implants. The pure Ti wires (Grade II, Baoji Haibao special metal materials Co., China) with diameter of 2 mm were cut into Ti rods ($\Phi2 \times L6$ mm^3) by a lining-cutting machine. The surfaces were ground with 600# and 1000# abrasive papers to wipe off the oxidized layer. The ground Ti rods were ultrasonically washed with acetone and distilled water and dried at 40 °C. After that, the prepared Ti rods were used as the Ti implants for the surface modification and animal surgery.

2.2. Surface Modification. In the MAO process, Ti implants ($\Phi2 \times L6$ mm^3) were used as anodes, and stainless steel plates were used as cathodes in an electrolytic bath. The electrolyte was prepared by dissolving Ca(CH$_3$COO)$_2$·H$_2$O (8.8 g·L^{-1}), Na$_2$SiO$_3$ (7.1 g·L^{-1}), Ca(H$_2$PO$_4$)$_2$·H$_2$O (6.3 g·L^{-1}), EDTA-2Na (15 g·L^{-1}), and NaOH (5 g·L^{-1}) into deionized water. The applied voltage, pulse frequency, duty cycle, and oxidizing time were set at 350 V, 600 Hz, 8.0%, and 5 min, respectively. In this way, the MAO coating containing Ca, P, Si, and Na was prepared on a Ti implant surface. The normal MAO coating

that covered the Ti implant was labeled as the N-MAO in the following.

For steam-hydrothermal treatment, the N-MAOs were hung up in the Teflon-lined autoclaves with Teflon-lined fixture, as we proposed in our previous work.[38] Only 10 mL of NaOH solution (0.1 mol·L^{-1}) was added into the autoclaves with the volume of 50 mL. Then, the autoclaves were kept at 200 °C for 24 h. After the steam-hydrothermal treatment, the prepared implants were collected and directly dried at 40 °C. In the following, the ST-MAO was used to label the MAO coating covered Ti implant after the steam-hydrothermal treatment.

For the post-heat treatment, the ST-MAOs were heated at 600 °C in air atmosphere condition for 1 h with the heating rate of 5 °C·min^{-1}, and the SHT-MAO was used to label the post-heated ST-MAO in this work.

2.3. Structure Characterization. *2.3.1. X-ray Diffraction (XRD).* The phase composition of the implants was analyzed by X-ray diffraction (D/max-γB, Rigaku Corporation, Japan) using Cu Kα radiation with a continuous scanning mode at a rate of 4° min^{-1}. The accelerating voltage and current were set at 40 kV and 50 mA.

2.3.2. X-ray Photoelectron Spectroscopy (XPS). X-ray photoelectron spectroscopy (K-Alpha, Thermofisher Scientific Co., USA) was used to detect the chemical compositions of the implant surfaces. In the XPS experiment, an Al Kα (1486.6 eV) X-ray source was used for the XPS work under a vacuum of 1.0×10^{-8} mbar. The current of X-ray beam was 6 mA, and the resolution for energy was 0.5 eV with a scanning step of 0.1 eV. The regions of 400 μm^2 on the sample surfaces were analyzed. The measured binding energies were calibrated by the C 1s (hydrocarbon C−C, C−H) of 284.6 eV, and the chemical states of O were analyzed.

2.3.3. Scanning Electron Microscopy (SEM) and Energy-Dispersive X-ray Spectrometer (EDS). Scanning electron microscopy (Helios Nanolab 600i, FEI Co., USA) was used to observe the surface morphology. In addition, the elemental concentrations of the implants were detected by an energy-dispersive X-ray spectrometer (EDAX, FEI Co., USA) equipped on the SEM system.

2.4. In Vivo Experiments. *2.4.1. Surgical Procedures.* All the animal experiments were approved by the animal care and experiment committee of the hospital affiliated with the Harbin Medical University. A total of 20 New Zealand rabbits with weight of 2.5−3 kg were used in the work. The rabbits were anaesthetized with 40 mg·kg^{-1} pentobarbital sodium via injecting into the ear vein. The legs were shaved, depilated, and disinfected with iodine. The rabbit was placed on a sterile drape to provide sterile conditions during surgery. After the tibia was exposed by skin incision, two holes ($\Phi2 \times L6$ mm^3) were drilled through the cortical bone in each tibia with tooth plant equipment under a cooling condition by saline water. After removing the bone chippings, four implants with different surface properties were placed in each rabbit (two implants per tibia), in order to reduce the influence of individual differences among rabbits (see in Figure S1 and S2 in the Supporting Information (SI)). Then the muscular fascia, subcutaneous tissue, and skin were sutured in sequence. After surgery, each rabbit was injected with an antibiotic of gentamicin by a dose of 1 mL per day for 3 days. The normal dietary intake by rabbit was performed, and a sutured line was removed after implantation for 10 days.

2.4.2. Sample Preparation. The rabbits were chosen randomly to be observed at two periods of 6 and 12 weeks after surgery. The chosen rabbits were sacrificed by the injection of air into the ear vein. Immediately, the tibia was detached from the rabbits for further treatment. Meanwhile, the remained organs were treated safely by the staff of the animal experiment center affiliated with the Harbin Medical University.

2.4.3. Radiographic Evaluation. The X-ray images of implants were taken by an X-ray digital photographic technique (UltralFocus100, Faxitron X-ray, USA) with power at 26 kV to examine the implantation status.

2.4.4. Micro-CT Test. The tibia implant specimens, fixed in 10% paraformaldehyde, were scanned using a micron X-ray 3D imaging system (Y. Cheetah, YXLON International GmbH, Germany) having an isotropic resolution of 7 μm. The growth of the biological tissue

and its interface structure around the implants were directly observed by three view profiles.

About micro-CT assessment of the biological tissue around implants, the data were analyzed by VG Studio 2.1V to rebuild the biological tissue around the implants in the region of interest (ROI) ($\Phi3 \times L6 - \Phi2 \times L6$ mm^3) as shown in Figure S3 in the SI. In each ROI, the following landmarks were used for morphometric measurement: (BTV) the biological tissue volume; (TV) the total volume; (BTSA) the biological tissue surface area.

2.4.5. Histological Evaluation. After fixation in 10% paraformaldehyde, the tibias containing the implants were dehydrated in a graded series of ethanol concentrations and subsequently embedded in methyl methacrylate resin (Technovit 7200 VLC, Exakt, Germany). Using a cutting-grinding unit (Apparatebau, Exakt, Germany) and starting from the major axis, blocks were cut and ground to a final thickness of approximately 50 μm.

For the double fluorescence labeling stain, the tetracycline hydrochloride (10 mg·mL^{-1}, 30 mg·kg^{-1}) and calcein (10 mg·mL^{-1}, 5 mg·kg^{-1}) were subcutaneously injected into the rabbits at different time of 40, 81 and 41, 82 days after surgery, respectively. The double fluorescence labeling stained sections were directly conducted on an OLYMPUS microscope (CXX41, OLYMPUS, Japan) with fluorescence light source, which were analyzed for evidence of bone regeneration.

Besides, the transverse histological sections were subjected to Van Gieson (VG) staining for bone histology analysis. The histological examination was performed under the OLYMPUS microscope (CXX41, OLYMPUS, Japan) with a normal light source. During bone remodeling, the micromotion of the placed implant caused by the frequent stress can stimulate the osteoclasts to resorb previously formed bone.[5−7] Therefore, the following landmarks were used for histomorphometric measurement of the bone tissue around the implant in the interested zone (IZ) (see Figure S4 in the SI): the percentages of bone tissue, soft tissue, and gap in the area of the VG stained region with a distance of 500 μm to the cylindrical surface of implants. ImageJ 1.48 software was used for image analyses.

2.4.6. Measurement of Push-Out Force for the Implants. The push-out test was carried out using a universal testing machine (Instron-1186, Instron Co., USA) with a penetrator in diameter of 1.8 mm. After the push-out test, the disrupted implants were immersed into 2.5% glutaraldehyde overnight. Then, the samples were washed by the phosphate-buffered saline (PBS) 3 times for 15 min and fixed by tannin for 1 h. The fixed samples were then washed by the PBS and dehydrated in graded ethanol solutions with the different concentrations of 50%, 70%, 90%, and 100% in sequence. The fracture surfaces of implants were examined by SEM for the failure mode analyses.

2.4.7. Statistical Analysis. Three rabbits were used for each of the *in vivo* micro-CT and histolocal analyses ($n = 3$), while six rabbits were used for the biomechanical push-out test at different time of 6 and 12 weeks after surgery. All of the data were expressed as means ± standard deviations. The statistical analysis was done by using the IBM SPSS statistical software package. The statistical significance of the difference was measured using a student analysis of variance. The P values <0.05 were considered a statistically significant difference.

3. RESULTS

Figure 1 shows the surface characteristics of the Ti implant, the MAO coating covered ones before and after steam-hydrothermal treatment, as well as the post-heat treatment one. The gross views showed that the smooth implants were completely covered by the coatings after different surface treatment routings (Figure 1(a)). As shown in Figure 1(b), mechanical grinding traces were observed from the SEM morphology of the Ti implant. Meanwhile, it was identified that the rough and porous surface morphology remained on the coatings, though different post processes were conducted on the MAO coating covered Ti implants (Figure 1(c), (d), and (e)). Interestingly,
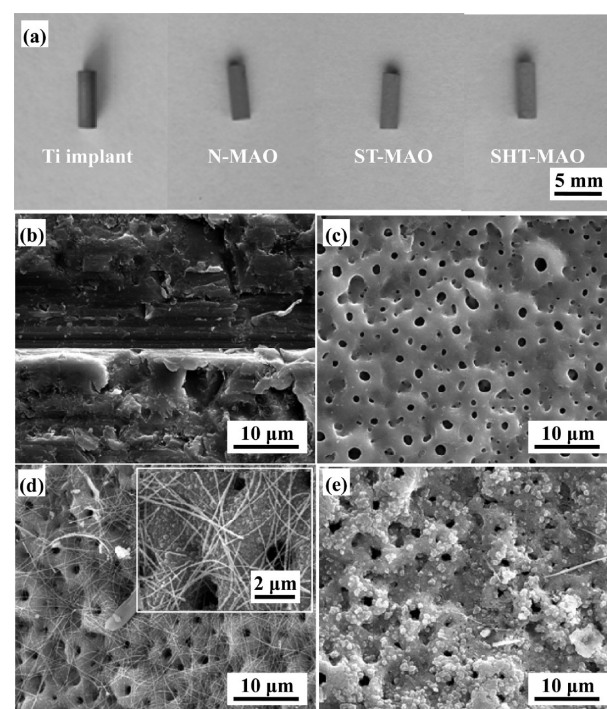

Figure 1. Surface characterization of the implants with gross views and SEM images: (a) gross views of the implants, (b) SEM image of the Ti implant, (c) SEM image of the N-MAO, (d) SEM image of the ST-MAO, and (e) SEM image of the SHT-MAO.

the surface of the ST-MAO was deposited with nanowires, also covered with nanoscale dots (Figure 1(d)). After the post-heat treatment, the surface of the SHT-MAO showed less in number but bigger in size nanodots with the absence of the nanowires (Figure 1(e)). This phenomenon indicates that post-heat treatment on the ST-MAO can promote the growth of the dot-like crystals on the coating surface but plays a damaging role in the nanowires.

Figure 2(a) shows the XRD patterns of the implants. The results revealed that the MAO coating mainly consisted of an amorphous phase with a small amount of anatase. After the steam-hydrothermal treatment, the characteristic peaks of HA at 31.8, 32.9, and 34.9° appeared on the XRD pattern of the ST-MAO. Meanwhile, the diffraction peak intensities of anatase at 25.7, 38.2, 53.9, and 55.0° were strongly enhanced as
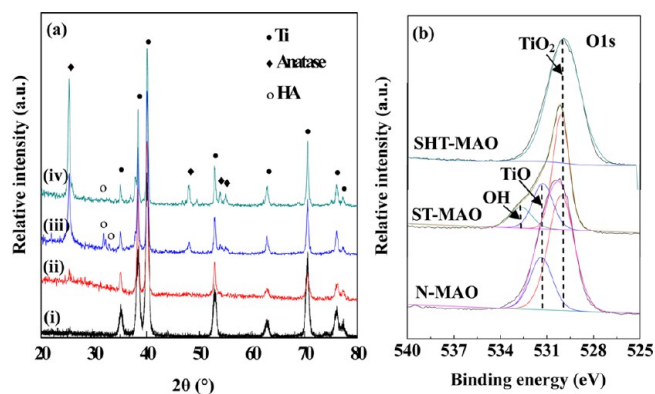

Figure 2. (a) XRD patterns of the implants: (i) Ti implant, (ii) N-MAO, (iii) ST-MAO, and (iv) SHT-MAO and (b) XPS spectra of the different coatings on Ti implants treated with different routings.
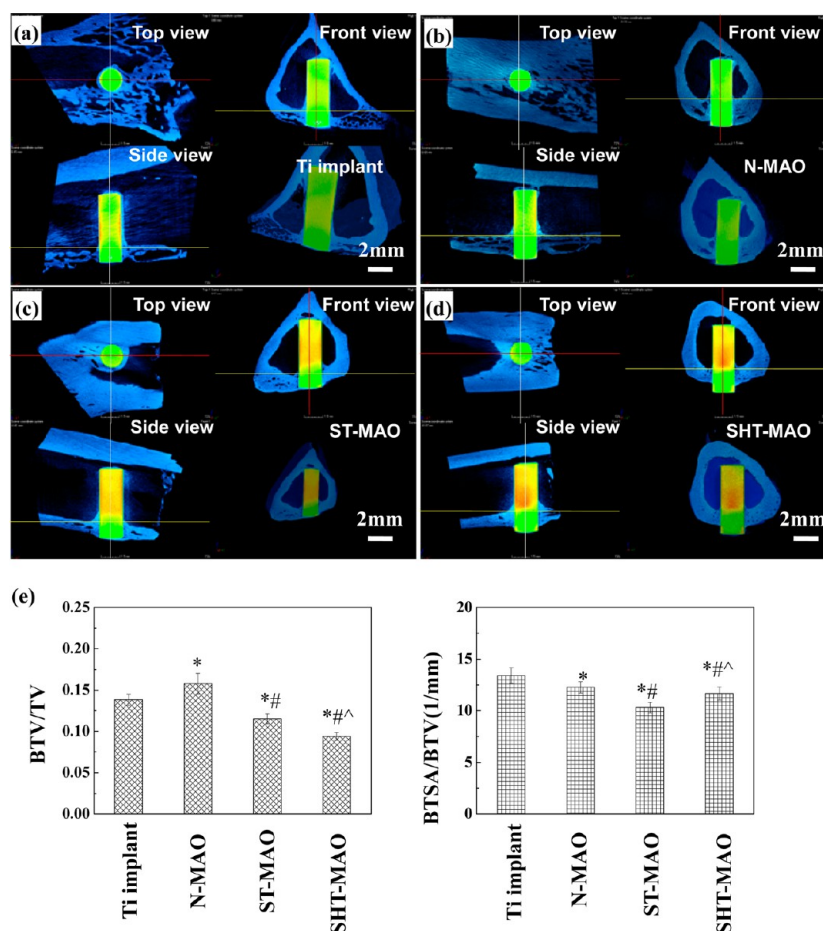
Figure 3. Micro-CT images and morphometric analyses of the implants after 12 weeks of healing: micro-CT images in three profiles for viewing of (a) the Ti implant, (b) N-MAO, (c) ST-MAO, (d) SHT-MAO, and (e) the statistical analysis of biological tissue in the ROI via micro-CT morphometry. $*p < 0.05$ compared to the Ti implant, $\#p < 0.05$ compared to the N-MAO, $\hat{p} < 0.05$ compared to the ST-MAO.

expected. In the case of the SHT-MAO, the characteristic peaks of anatase exhibited the strongest intensity among the XRD patterns, but the peaks of HA almost disappeared. Associated with the SEM results, we can confirm that the nanodot is anatase, and the nanowires can be identified as HA, which is consistent with TEM and FT-IR results of the as-prepared Ti plate reported in our previous work.[38]

Figure 2(b) shows the XPS spectra detected from the surfaces of the different coatings covered Ti implants. According to the literature,[31,41−46] the original O 1s spectrum of the N-MAO could be divided into two Gaussian peaks, which were assigned to TiO_2 (anatase) at 530.1 eV[31,41−44] and oxide with lower oxidation state (like TiO) at 531.8 eV,[41] respectively (Figure 2(b)). After the steam hydrothermal treatment, a third peak of O 1s at 532.8 eV was also detected from the surface of the ST-MAO, indicating the incorporation of basic hydroxyl and physical bound water.[45,46] Associated with our previous work,[38] the incorporated basic hydroxyl should be attributed to the formation of HA and Ti−OH on the surface of ST-MAO. However, only the peak at 530.1 eV remained in the spectrum of the SHT-MAO. This is consistent with the XRD and SEM results, indicating further oxidation of the ST-MAO surface.

The micro-CT-based biologically morphologic and morphometric analyses preformed at week 12 of healing in the rabbit tibia model revealed a sharp contrast in osteogenic behavior around implants with different surface chemistry and topologic structure. Representative cross-sectional micro-CT images obtained from the three profiles are shown in Figure 3. In general (in the side view), the cortical bones in the side without implants still remained a dense structure. However, cortical bones near the implanted Ti implant and N-MAO showed loose structure, while those near the ST-MAO and SHT-MAO exhibited relatively dense structure. Similar results have been observed from the transitional zone between the cortical bone and bone marrow (top view). The induced biological tissue showed point-like contact around the Ti implant surface. In the case of the N-MAO, more biological tissue was formed around the transitional zone, which partly continuously contacted with the N-MAO surface. As for the ST-MAO and SHT-MAO, the implant surface in the transitional zone was completely covered by the biological tissue, which exhibited ring-like contact. Separately statistical analyses for the ROI (Figure 3(e)) demonstrated that the biological tissue volume was significantly greater around the Ti implant and N-MAO than around the ST-MAO and SHT-MAO ($p < 0.05$), while the biological tissues around the Ti implant and N-MAO show a high value in BTSA/BTV indicating the loose structure ($p < 0.05$). In terms of ST-MAO and SHT-MAO, a smaller amount of biological tissue but with dense structure was formed around the implants ($p < 0.05$).

After identifying that there was more biological tissue formed on the regions of interest around the Ti implant and the N-MAO, we performed histological morphometry to determine
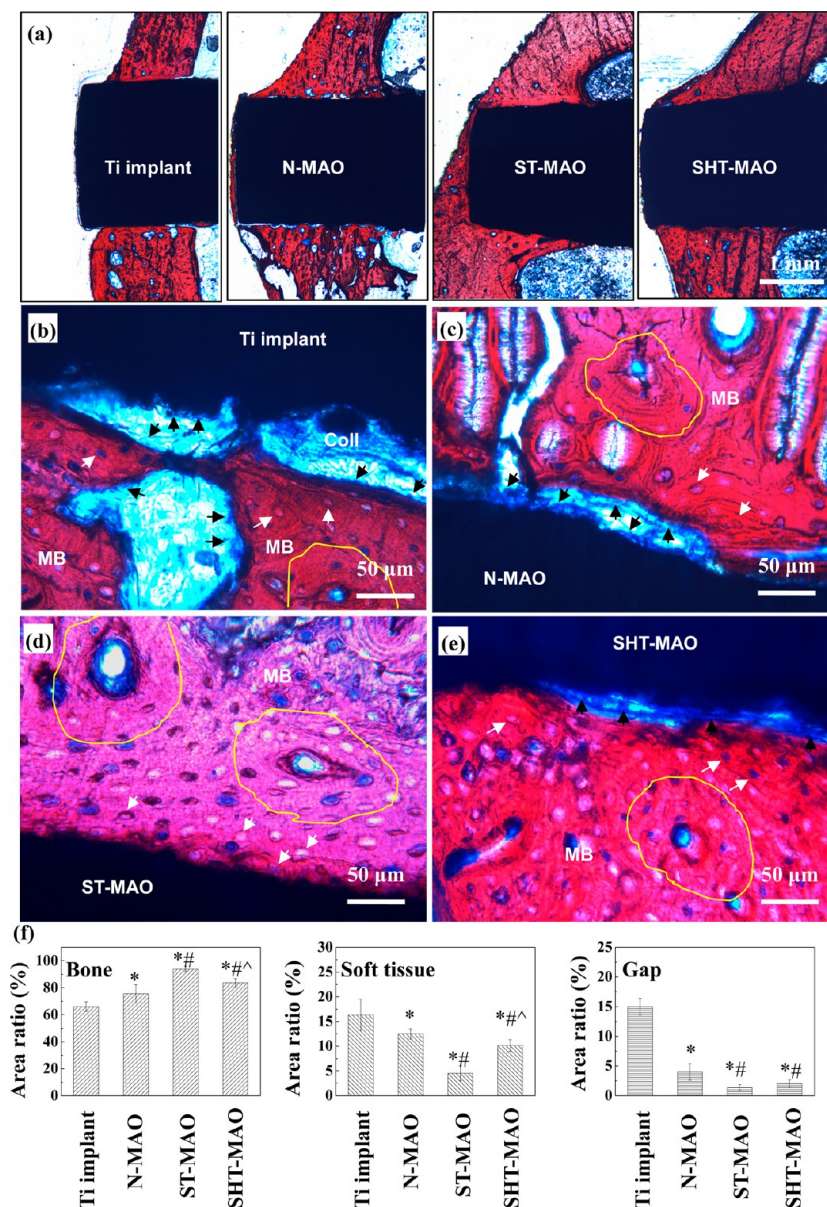
Figure 4. Bone histology and histomorphometry around the implants after 12 weeks of healing: (a) gross histological views of the implants in the region of cortical bone, the representative histological morphology of (b) the Ti implant, (c) N-MAO, (d) ST-MAO and (e) SHT-MAO, and (f) the histomorphometry analysis of mineralized bone, soft tissue and gap in the interested zoon. (MB) mineralized bone; (black arrow) osteoblasts; (white arrow) osteocytes; (Coll) collagen birefringence; (yellow ring) osteon. *$p < 0.05$ compared to the Ti implant, #$p < 0.05$ compared to the N-MAO, $\hat{p} < 0.05$ compared to the ST-MAO.

whether this increase was caused by the increased osteogenesis (Figure 4).

After implantation for 12 weeks, new bone formation was found to have occurred concentrically around all implant surfaces (Figure 4(a)). The amount of newly formed bone appeared to be greater around both the ST-MAO and SHT-MAO than that of the Ti implant and N-MAO. Magnified images around the Ti implant surface revealed that most of the peri-implant bone was separated from the implant surface by soft tissues, preventing a direct bone–implant contact (Figure 4(b)). In contrast, the N-MAO surfaces, part of the peri-implant bone, were in direct contact with the implant surface, while the other part was invaded by soft tissue at the implant interface (Figure 4(c)). Fortunately, the surface of the ST-MAO exhibited excellent direct bone–implant contact in the cortical region (Figure 4(d)). Although direct bone–implant

contact was found around both the ST-MAO and SHT-MAO surfaces (Figure 4(e)), some bone tissue on the SHT-MAO surface remained infiltrated with soft tissue. It was noticed that the infiltrated soft tissue appeared to be thinner around the SHT-MAO than around the N-MAO surfaces.

The histomorphometric results are shown in Figure 4(f). The area ratio of bone in the VG stained regions was consistently higher for coating-covered implant surfaces than for the Ti implant surface ($p < 0.05$). In contrast, area ratios of soft tissue and gap were substantially lower for coating-covered implant surfaces than for the Ti implant surface ($p < 0.05$). Among the different coating covered implants, the N-MAO showed the lowest area ratio of bone, while the ST-MAO exhibited the highest bone area ratio of 92.1% ($p < 0.05$). Additionally, there was no significant difference in gap ratio

between ST-MAO and SHT-MAO ($p = 0.07$). This result is consistent with the histological morphology.

Since we did not find any decisive differences between ST-MAO and SHT-MAO in histological and histomorphometric analyses, possible differences might exist in the interfacial tissue at different healing time. Thus, the histological images around the ST-MAO and SHT-MAO with double fluorescence labeling at different healing time of 6 and 12 weeks were examined (Figure 5).
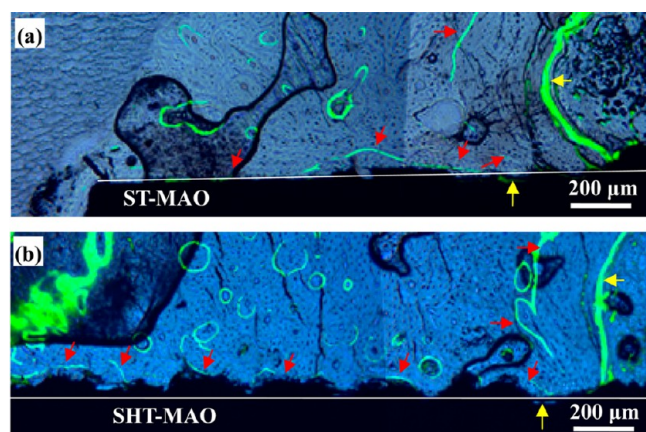

Figure 5. Histological images around the implants with double fluorescence labeling at different healing time of 6 and 12 weeks: (a) the ST-MAO and (b) SHT-MAO. (Red arrow) 6 weeks fluorescence labeled line; (yellow arrow) 12 weeks fluorescence labeled line; (white line) the ideal interface between implant and bone tissue.

As observed from Figure 5, the green fluorescence lines labeled by red arrows point to the osteoblast formed at 41 days (6 weeks), while the yellow ones correspond to the osteoblast formed at 82 days (12 weeks). It was clear that the bone tissue did not contact well with the surface of both the ST-MAO and SHT-MAO after healing of 6 weeks. Though the direct bone–implant contact was observed at the ST-MAO surface, near half of the interface in the cortical region was still separated by soft tissue or gaps. Unfortunately, direct bone–implant contact on the surface of the SHT-MAO was also rarely seen, which showed a wave-like fluorescence line at the interface separated by a soft tissue or gaps. At 12 weeks after the surgery, both the ST-MAO and the SHT-MAO were well covered by bone tissue (synostosis). This is consistent with the VG stained histological images. Meanwhile, it is noticed that the amount of the as-formed bone around the ST-MAO in the transitional region is more than that around the SHT-MAO, indicating the excellent bone regeneration capability for the ST-MAO.

Figure 6 shows the push-out forces for the Ti implant, N-MAO, ST-MAO, and SHT-MAO after different healing time of 6 and 12 weeks. The push-out force was different between the four implant groups due to the differences in surface chemistry and topologic structure. After surgery for 6 weeks (Figure 6(a)), the push-out force for the Ti implant was about 2.3 N, while that for the N-MAO was enhanced to about 74.3 N ($p <$ 0.05). Interestingly, the ST-MAO displayed greater improvement in the push-out force compared to the N-MAO, which was over 2 times that of the N-MAO (157.0 N) ($p < 0.05$). At the same time, it was noticed that the push-out force for the SHT-MAO was about 80% that of the ST-MAO (124.6 N) ($p < 0.05$). Although the difference between the four implant groups remained significant at week 12 ($p < 0.05$), a different
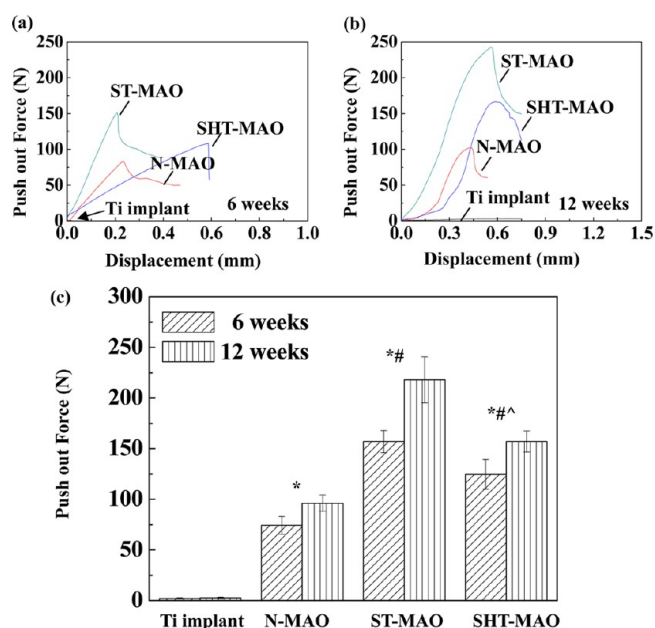

Figure 6. Representative displacement curves and push-out force of the implants at different healing time of 6 and 12 weeks: (a) the representative displacement curves of the implants after 6 weeks of healing, (b) the representative displacement curves of the implants after 12 weeks of healing, (c) the push-out force of the implants. *$p <$ 0.05 compared to the Ti implant, #$p < 0.05$ compared to the N-MAO, $\hat{p} < 0.05$ compared to the ST-MAO.

pattern of change was observed from week 6 to 12 (Figure 6(c)). The push-out force of the Ti implant remained unchanged from week 6 to 12, while the push-out force of the different coatings-covered ones significantly increased during this time period ($p < 0.05$). These results indicate that the functional group and nanotopologic structure on the modified MAO coating surface could improve the push-out force and benefit osseointegration of the implants.

Typical SEM images of the ST-MAO and SHT-MAO retrieved at week 12 are presented in Figure 7, from which remnants of biological structures are seen on both the ST-MAO and SHT-MAO surface. Representative SEM images of the cortical and transitional regions are investigated together with the EDS spot scans. In the cortical region, remnants of mineral bone (Ca 9.2 at. % and P 5.5 at. %) were observed from the magnified SEM images (Figure 7(e) and (f)). Meanwhile, it was clear that some part of the coating on the ST-MAO has been pulled off with the bone tissue (Ti 88.2 at. % and C 11.8 at. %) (Figure 7(g)). This phenomenon indicates the synostosis in the cortical region. In contrast, the local area without tissue connecting was observed from the surface of SHT-MAO, though the majority of the cortical region on the implant surface showed pulled-off coating and remnants of mineral bone (Figure 7(d)). This indicated that the implant in this local area had slid and detached from the tissue during the push-out test attributed to the soft tissue connection. Thus, the push-out force of the SHT-MAO between the implant surface and biological tissue was lower than that of ST-MAO. The excellent biomechanical property of ST-MAO would be attributed to the intimate bonding with mineral bone. Besides, the facture in the transitional regions of both the ST-MAO and the SHT-MAO occurred at the bone tissue side, leaving the biological tissue on the implant surfaces (Figure 7(i) and (j)). This phenomenon should be attributed to the structure of newly formed bone
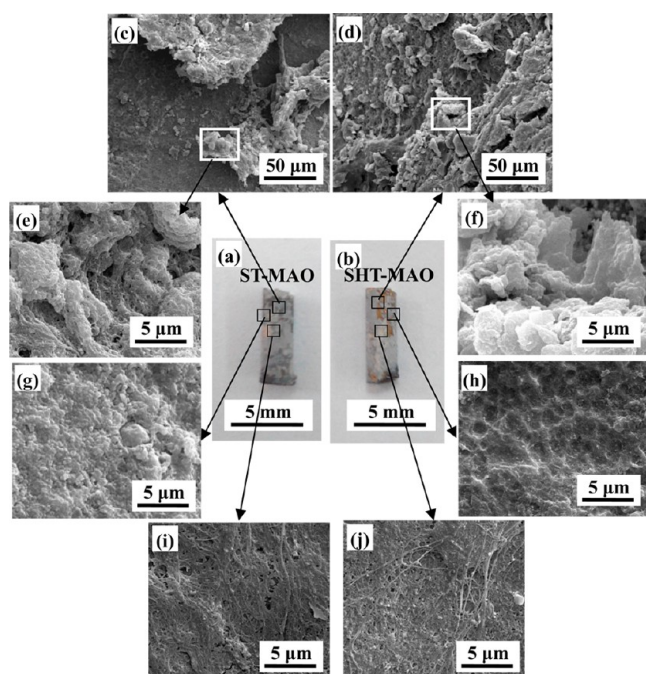
Figure 7. Surface characterization of the pushed-out ST-MAO and SHT-MAO at 12 weeks of healing with gross views and SEM images: (a,b) gross views of the pushed-out implants, (c,d) representative SEM images of entice implant surfaces with biological bonding structures at the cortical bone region, (e,f) magnified morphology of the formed mineral bone, (g,h) magnified morphology of the coating pulled off area, and (i,j) representative SEM images of entice implant surfaces at the transitional region for the ST-MAO and SHT-MAO, respectively.

(partly mineralized collagen fiber (Ca 3.2 at. % and P 1.8 at. %), which cannot bear the load.

4. DISCUSSION

Both the surface chemistry and topologic structure of the MAO coating on implants have been modified by the post treatments in this work. Results show that obvious differences in osseointegration (biological tissue volume in the region of interest calculated by micro-CT and bone—implant contact at the interface analyzed by histological images) are obtained among the implants with various surface functional structures, which are fabricated through different routings. As for the histological image analysis (Figure 4), the ST-MAO shows a significantly higher rate of bone formation as compared to the Ti implant and the N-MAO; thus, it exhibits high levels of osseointegration as exemplified by a direct bone—implant contact observed in the histological sections. In contrast, the N-MAO shows significantly lower volume of regenerated bone and little direct bone—implant contacted interface due to soft tissue formation (Figure 4). Unfortunately, the Ti implant shows poor bone—implant contact at the interface, which is separated by soft tissues and gaps (Figure 4). The SHT-MAO surface shows some direct bone—implant contact but also some formation of soft tissue, which is situated in between the N-MAO and ST-MAO (Figure 4). Meanwhile, the push-out force for the implants is in line with the bone—implant contact of the surface (Figure 6).

One unexpected observation is that the implants integrated with loose cortical bone show large volume of biological tissue in the region of interest calculated by micro-CT (Figure 3), i.e., Ti implant and the N-MAO. This would be attributed to the

soft tissue which cannot be distinguished from the bone tissue (biological tissue) owing to the artifact caused by the edge of the implant. Namely, the biological tissue around the Ti implant at the transitional and bone marrow level is soft tissue. It is generally assumed that a large volume of biological tissue around the N-MAO is also due to the formation of soft tissue.

Herein, osseointegration directly dominates the push-out force of the implants, while it can be affected by many factors.[47−54] Normally, osseointegration between the implant and bone tissue involves two major steps: the formation of a carbonated hydroxyapatite on the surface via ion exchange, and then the collagen fibers of the host bone insert into the carbonated apatite layer.[8] Corresponding to multiple comparisons of the differences between the four group implants fabricated by different routings, the differences in osseointegration can be explained in terms of the distinct differences of the topographical and chemical properties.

Previous investigations reveal that the Ti implant is not rejected by the body, which demonstrates intimate integration with the host bone tissue.[4] This is attributed to the formed titanate (e.g., Na_2TiO_3) on the surface via ion exchange during the long-term implantation (12 months), which can trigger carbonated apatite nucleation. Herein, like most of the bioinert device, a capsule is formed around the Ti implant's foreign body after surgery for 12 weeks (short-term implantation) (Figure S5 in the SI), owing to the perfectly natural defense mechanism.[55]

On the basis of the quantitative and qualitative comparisons of the surface characteristics between the Ti implant and the N-MAO, the improved osseointegration of the MAO coating covered implant is most likely due to the topographical properties (increased surface roughness and/or porous structure) but not the incorporated Ca and P elements owing to the poor apatite-inducing ability based on our previous work,[22] and the porous surface structure can contribute to higher bone inducing protein adsorption,[24] which supports our point here.

Furthermore, Gittens et al. suggest that surface nanoscale roughness, which directly corresponds to the sizes of proteins and cell membrane receptors, could play an important role in osteoblast differentiation and tissue regeneration.[56−58] Consistent with their point, the SHT-MAO shows the better osseointegration than that of the N-MAO, due to the formation of nanodots on the porous coating surfaces.

Moreover, the chemistry of coating is another key factor for the enhanced osseointegration. It is clear that the HA and Ti—OH group are formed on the surface of the ST-MAO, which can trigger the formation of a carbonated hydroxyapatite.[19,21] Meanwhile, the nanowires and nanodots can stimulate the receptor on the cell surface of osteoblast to promote proliferation and differentiation.[24] Thus, the ST-MAO shows excellent osseointegration at the bone—implant interface since it combines the interests of both the topographical and chemical properties to satisfactorily meet the two major steps for the bone bonding mechanism. The substantially enhanced bone generation around the ST-MAO and the results of the push-out test confirm these predictions.

Taking the results together, the ST-MAO associated with the benefits of both nanotopologic structure and functional group has been demonstrated to be a potentially effective way to improve the degree and rate of bone—implant integration. Thus, the steam-hydrothermal treatment on the MAO coating

covered Ti implant would be a promising strategy to fabricate the next generation of advanced Ti-based implants.

5. CONCLUSION

The surface properties of the MAO coating covered Ti implant have been mediated by post surface treatments, particularly, the steam-hydrothermal treatment and heat treatment. The significantly improved osseointegration as evaluated by biomechanical and histomorphometrical techniques after implant insertion can be explained by the differences in surface chemistry and topologic structure. Thanks to the microscale porous surface structure, the biocompatibility and biomechanical property of the MAO coating covered Ti implant have been obviously improved when compared with that of the Ti implant. In contrast, the hierarchical surface structure (nanoscale dots on microscale porous surface) obtained by post treatments directly enhances the bone regeneration around implant surfaces, resulting in excellent push-out force. The differences in surface chemistry point out that the as-generated Ti−OH and HA based on the MAO coating containing Ca, P, Si and Na can effectively benefit from the bonding between bone and implant when compared with that of the one simply covered with hierarchically topologic coating. Therefore, the steam-hydrothermal treatment for the MAO coating covered Ti implant should be an effective approach for improving the performance of endosseous implants since it combines the benefits of both hierarchical structure and functional group of the implant surface.

ASSOCIATED CONTENT

S **Supporting Information**

Schematic diagrams for the animal surgery, micro-CT-based biologically morphometric analysis and histological morphometry of the VG stained sections; X-ray radiographs of the implants after different healing times of 6 and 12 weeks and the surface morphology and EDS spectrum of the pushed-out Ti implant after healing of 12 weeks. This material is available free of charge via the Internet at http://pubs.acs.org.

AUTHOR INFORMATION

Corresponding Author

*E-mail: daqingwei@hit.edu.cn. Fax: +86-451-8641-4291. Tel.: +86-451-8640-2040-8403.

Notes

The authors declare no competing financial interest.

Ethical Approval. For animal studies: The animal care and experiment ethics committee of the Harbin Medical University approved this study and supervised all animal experiments in this study.

ACKNOWLEDGMENTS

REFERENCES

(1) Wu, S. L.; Liu, X. M.; Yeung, K. W. K.; Liu, C. S.; Yang, X. J. Biomimetic Porous Scaffolds for Bone Tissue Engineering. *Mater. Sci. Eng., R* **2014**, *80*, 1−36.

(2) Chen, Q. Z.; Thouas, G. A. Metallic Implant Biomaterials. *Mater. Sci. Eng., R* **2015**, *87*, 1−57.

(3) Steflik, D. E.; Corpe, R. S.; Young, T. R.; Sisk, A. L.; Parr, G. R. The Biologic Tissue Responses to Uncoatedand Coated Implanted Biomaterials. *Adv. Dent. Res.* **1999**, *13*, 27−33.

(4) Fujibayashi, S.; Neo, M.; Kim, H. M.; Kokubo, T.; Nakamura, T. Osteoinduction of Porous Bioactive Titanium Metal. *Biomaterials* **2004**, *25*, 443−450.

(5) Nasab, M. B.; Hassan, M. R.; Sahari, B. B. Metallic Biomaterials of Knee and Hip − A Review. *Trends Biomater. Artif. Organs* **2010**, *24*, 69−82.

(6) Mulari, M. T. K.; Qu, Q.; Harkonen, P. L.; Vaananen, H. K. Osteoblast-Like Cells Complete Osteoclastic Bone Resorption and Form New Mineralized Bone Matrix *in vitro*. *Calcif. Tissue Int.* **2004**, *75*, 253−261.

(7) Mori, S.; Burr, D. B. Increased Intracortical Remodeling Following Fatigue Damage. *Bone* **1993**, *14*, 103−109.

(8) Maquart, F. X.; Bellon, G.; Chaqour, B.; Wegrowski, J.; Patt, L. M.; Trachy, R. E.; Monboisse, J. C.; Chastang, F.; Birembaut, P.; Gillery, P.; Borel, J. P. *In vivo* Stimulation of Connective Tissue Accumulation by The Tripeptide-Copper Complex Glycyl-L-Histidyl-L-Lysine-Cu^{2+} in Rat Experimental Wounds. *J. Clin. Invest.* **1993**, *92*, 2368−2376.

(9) Ryan, G.; Pandit, A.; Apatsidis, D. P. Fabrication Methods of Porous Metals for Use in Orthopaedic Applications. *Biomaterials* **2006**, *27*, 2651−2670.

(10) Tsui, Y. C.; Doyle, C.; Clyne, T. W. Plasma Sprayed Hydroxyapatite Coatings on Titanium Substrates Part 1: Mechanical Properties and Residual Stress Levels. *Biomaterials* **1998**, *19*, 2015−2029.

(11) Zhang, W. G.; Liu, W. M.; Liu, Y.; Wang, C. T. Tribological Behaviors of Single and Dual Sol-Gel Ceramic Films on Ti-6Al-4V. *Ceram. Int.* **2009**, *35*, 1513−1520.

(12) Wang, X. X.; Hayakawa, S.; Tsuru, K.; Osaka, A. Bioactive Titania Gel Layers Formed by Chemical Treatment of Ti Substrate with A H_2O_2/HCl Solution. *Biomaterials* **2002**, *23*, 1353−1357.

(13) Yen, S. K.; Lin, C. M. Cathodic Reactions of Electrolytic Hydroxyapatite Coating on Pure Titanium. *Mater. Chem. Phys.* **2002**, *77*, 70−76.

(14) Kuo, M. C.; Yen, S. K. The Process of Electrochemical Deposited Hydroxyapatite Coatings on Biomedical Titanium at Room Temperature. *Mater. Sci. Eng., C* **2002**, *20*, 153−160.

(15) Zhitomirsky, I.; Gal-Or, L. Electrophoretic Deposition of Hydroxyapatite. *J. Mater. Sci.: Mater. Med.* **1997**, *8*, 213−219.

(16) Lee, E. J.; Shin, D. S.; Kim, H. E.; Kim, H. W.; Koh, Y. H.; Jang, J. H. Membrane of Hybrid Chitosan-Silica Xerogel for Guided Bone Regeneration. *Biomaterials* **2009**, *30*, 743−750.

(17) Hamada, K.; Kon, M.; Hanawa, T.; Yokoyama, K.; Miyamoto, Y.; Asaoka, K. Hydrothermal Modification of Titanium Surface in Calcium Solutions. *Biomaterials* **2002**, *23*, 2265−2272.

(18) Suh, J. Y.; Jang, B. C.; Zhu, X.; Ong, J. L.; Kim, K. Effect of Hydrothermally Treated Anodic Oxide Films on Osteoblast Attachment and Proliferation. *Biomaterials* **2003**, *24*, 347−355.

(19) Liu, F.; Song, Y.; Wang, F.; Shimizu, T.; Igarashi, K.; Zhao, L. Formation Characterization of Hydroxyapatite on Titanium by Microarc Oxidation and Hydrothermal Treatment. *J. Biosci. Bioeng.* **2005**, *100*, 100−104.

(20) Tsai, C. C.; Nian, J. N.; Teng, H. Mesoporous Nanotube Aggregates Obtained from Hydrothermally Treating TiO_2 with NaOH. *Appl. Surf. Sci.* **2006**, *253*, 1898−1902.

(21) Zhou, J. H.; Han, Y. Effect of Hydrothermal Treatment Model on The Formation of Sr-HA Nanorod Arrays on Microarc Oxidized Titania Coatings. *Appl. Surf. Sci.* **2013**, *286*, 384−390.

(22) Zhou, R.; Wei, D. Q.; Feng, W.; Cheng, S.; Yang, H. Y.; Li, B. Q.; Wang, Y. M.; Jia, D. C.; Zhou, Y. Bioactive Coating with

Hierarchical Double Porous Structure on Titanium Surface Formed by Two-Step Microarc Oxidation Treatment. *Surf. Coat. Technol.* **2014**, *252*, 148−156.

(23) Yuan, H.; Kurashina, K.; de Bruijn, J. D.; Li, Y.; de Groot, K.; Zhang, X. A Preliminary Study on Osteoinduction of Two Kinds of Calcium Phosphate Ceramics. *Biomaterials* **1999**, *20*, 1799−1806.

(24) Gittens, R. A.; McLachlan, T.; Olivares-Navarrete, R.; Cai, Y.; Berner, S.; Tannenbaum, R.; Schwartz, Z.; Sandhage, K. H.; Boyan, B. D. The Effects of Combined Micron-/Submicron-Scale Surface Roughness and Nanoscale Features on Cell Proliferation and Differentiation. *Biomaterials* **2011**, *32*, 3395−3403.

(25) Pang, J.; Sjostrom, T.; Dynmock, D.; Su, B. Adhesion of Streptococcus Mitis and Fusobacterium Nucleatum on Nanopatterned Titanium Surfaces. *Bioinspired, Biomimetic Nanobiomater.* **2013**, *2*, 117−122.

(26) Cai, K. Y.; Bossert, J.; Jandt, K. D. Does The Nanometre Scale Topography of Titanium Influence Protein Adsorption and Cell Proliferation? *Colloids Surf., B* **2006**, *49*, 136−144.

(27) Sjostrom, T.; McNamara, L. E.; Meek, R. M. D.; Dalby, M. J.; Su, B. 2D and 3D Nanopatterning of Titanium for Enhancing Osteoinduction of Stem Cells at Implant Surfaces. *Adv. Healthcare Mater.* **2013**, *2*, 1285−1293.

(28) Yan, Y. Y.; Sun, J. F.; Han, Y.; Li, D. C.; Cui, K. Microstructure and Bioactivity of Ca, P and Sr Doped TiO_2 Coating Formed on Porous Titanium by Micro-Arc Oxidation. *Surf. Coat. Technol.* **2010**, *205*, 1702−1713.

(29) Ishizawa, H.; Fujino, M.; Ogino, M. Histomorphometric Evaluation of The Thin Hydroxyapatite Layer Formed Through Anodization Followed by Hydrothermal Treatment. *J. Biomed. Mater. Res.* **1997**, *35*, 199−206.

(30) Yerokhin, A. L.; Nie, X.; Leyland, A.; Matthews, A.; Dowey, S. J. Plasma Electrolysis for Surface Engineering. *Surf. Coat. Technol.* **1999**, *122*, 73−93.

(31) Han, Y.; Chen, D. H.; Sun, J. F.; Zhang, Y. M.; Xu, K. W. UV-Enhanced Bioactivity and Cell Response of Micro-Arc Oxidized Titania Coatings. *Acta Biomater.* **2008**, *4*, 1518−1529.

(32) Krupa, D.; Baszkiewicz, J.; Zdunek, J.; Sobczak, J. W.; Lisowski, W.; Smolik, J.; Slomka, Z. Effect of Plasma Electrolytic Oxidation in The Solutions Containing Ca, P, Si, Na on The Properties of Titanium. *J. Biomed. Mater. Res., Part B* **2012**, *100*, 2156−2166.

(33) Han, Y.; Hong, S. H.; Xu, K. Structure and *in vitro* Bioactivity of Titania-Based Films by Micro-Arc Oxidation. *Surf. Coat. Technol.* **2003**, *168*, 249−258.

(34) Song, W. H.; Jun, Y. K.; Han, Y.; Hong, S. C. Biomimetic Apatite Coatings on Micro-Arc Oxidized Titania. *Biomaterials* **2004**, *25*, 3341−3349.

(35) Krupa, D.; Baszkiewicz, J.; Zdunek, J.; Smolik, J.; Słomka, Z.; Sobczak, J. W. Characterization of The Surface Layers Formed on Titanium by Plasma Electrolytic Oxidation. *Surf. Coat. Technol.* **2010**, *205*, 1743−1749.

(36) Nishiguchi, S.; Kato, H.; Fujita, H.; Oka, M.; Kim, H. M.; Kokubo, T.; Nakamura, T. Titanium Metals Form Direct Bonding to Bone after Alkali and Heat Treatments. *Biomaterials* **2001**, *22*, 2525−2533.

(37) Kim, H. M.; Miyaji, F.; Kokubo, T.; Nakamura, T. Preparation of Bioactive Ti and Its Alloys via Simple Chemical Surface Treatment. *J. Biomed. Mater. Res.* **1996**, *32*, 409−417.

(38) Zhou, R.; Wei, D. Q.; Cao, J. Y.; Feng, W.; Cheng, S.; Du, Q.; Li, B. Q.; Wang, Y. M.; Jia, D. C.; Zhou, Y. The Effect of NaOH Concentration on The Steam-Hydrothermally Treated Bioactive Microarc Oxidation Coatings Containing Ca, P, Si and Na on Pure Ti Surface. *Mater. Sci. Eng., C* **2015**, *49*, 669−680.

(39) Xu, X. M.; Wang, J. F.; Tian, J. T.; Wang, X.; Dai, J. H.; Liu, X. Y. Hydrothermal and Post-Heat Treatments of TiO_2/ZnO Composite Powder and Its Photodegradation Behavior on Methyl Orange. *Ceram. Int.* **2011**, *37*, 2201−2206.

(40) Yoshida, R.; Suzuki, Y.; Yoshikawa, S. Syntheses of TiO_2(B) Nanowires and TiO_2 Anatase Nanowires by Hydrothermal and Post-Heat Treatments. *J. Solid State Chem.* **2005**, *178*, 2179−2185.

(41) Zhou, R.; Wei, D. Q.; Cheng, S.; Li, B. Q.; Wang, Y. M.; Jia, D. C.; Zhou, Y.; Guo, H. F. The Structure and *in vitro* Apatite Formation Ability of Porous Titanium Covered Bioactive Microarc Oxidized TiO_2-Based Coatings Containing Si, Na and Ca. *Ceram. Int.* **2014**, *40*, 501−509.

(42) Viornery, C.; Chevolot, Y.; Léonard, D.; Aronsson, B. O.; Péchy, P.; Mathieu, H. J.; Descouts, P.; Grätzel, M. Surface Modification of Titanium with Phosphonic Acid to Improve Bone Bonding: Characterization by XPS and ToFSIMS. *Langmuir* **2002**, *18*, 2582−2589.

(43) Sham, T. K.; Lazarus, M. S. X-Ray Photoelectron Spectroscopy (XPS) Studies of Clean and Hydrated TiO_2 (Rutile) Surfaces. *Chem. Phys. Lett.* **1979**, *68*, 426−432.

(44) Zhou, R.; Wei, D. Q.; Ke, H.; Cao, J. Y.; Li, B. Q.; Cheng, S.; Feng, W.; Wang, Y. M.; Jia, D. C.; Zhou, Y. $H_2Ti_5O_{11} \cdot H_2O$ Nanorod Arrays Formed on Ti Surface via A Hybrid Technique of Microarc Oxidation and Chemical Treatment. *CrystEngComm* **2015**, *17*, 2705−2717.

(45) Kasuga, T.; Kondo, H.; Nogami, M. Apatite Formation on TiO_2 in Simulated Body Fluid. *J. Cryst. Growth* **2002**, *235*, 235−240.

(46) Camposeco, R.; Castillo, S.; Mejia, I.; Mugica, V.; Carrera, R.; Montoya, A.; Morán-Pineda, M.; Navarrete, J.; Gómez, R. Active TiO_2 Nanotubes for CO Oxidation at Low Temperature. *Catal. Commun.* **2012**, *17*, 81−88.

(47) Tada, S.; Timucin, E.; Kitajima, T.; Sezerman, O. U.; Ito, Y. Direct *in vitro* Selection of Titanium-Binding Epidermal Growth Factor. *Biomaterials* **2014**, *35*, 3497−3503.

(48) Qin, H.; Cao, H. L.; Zhao, Y. C.; Zhu, C.; Cheng, T.; Wang, Q. J.; Peng, X. C.; Cheng, M. Q.; Wang, J. X.; Jin, G. D.; Jiang, Y.; Zhang, X. L.; Liu, X. Y.; Chu, P. K. *In vitro* and *in vivo* Anti-Biofilm Effects of Silver Nanoparticles Immobilized on Titanium. *Biomaterials* **2014**, *35*, 9114−9125.

(49) Jin, G. D.; Qin, H.; Cao, H. L.; Qian, S.; Zhao, Y. C.; Peng, X. C.; Zhang, X. L.; Liu, X. Y.; Chu, P. K. Synergistic Effects of Dual Zn/Ag Ion Implantation in Osteogenic Activity and Antibacterial Ability of Titanium. *Biomaterials* **2014**, *35*, 7699−7713.

(50) Ueno, T.; Yamada, M.; Suzuki, T.; Minamikawa, H.; Sato, N.; Hori, N.; Takeuchi, K.; Hattori, M.; Ogawa, T. Enhancement of Bone−Titanium Integration Profile with Uv-Photofunctionalized Titanium in A Gap Healing Model. *Biomaterials* **2010**, *31*, 1546−1557.

(51) Ehrensberger, M. T.; Tobias, M. E.; Nodzo, S. R.; Hansen, L. A.; Luke-Marshall, N. R.; Cole, R. F.; Wild, L. M.; Campagnari, A. A. Cathodic Voltage-Controlled Electrical Stimulation of Titanium Implants as Treatment for Methicillin-Resistant Staphylococcus Aureus Periprosthetic Infections. *Biomaterials* **2015**, *41*, 97−105.

(52) Ma, Q. L.; Zhao, L. Z.; Liu, R. R.; Jin, B. Q.; Song, W.; Wang, Y.; Zhang, Y. S.; Chen, L. H.; Zhang, Y. M. Improved Implant Osseointegration of A Nanostructured Titanium Surface via Mediation of Macrophage Polarization. *Biomaterials* **2014**, *35*, 9853−9867.

(53) Li, X.; Ma, X. Y.; Feng, Y. F.; Ma, Z. S.; Wang, J.; Ma, T. C.; Qi, W.; Lei, W.; Wang, L. Osseointegration of Chitosan Coated Porous Titanium Alloy Implant by Reactive Oxygen Species-Mediated Activation of The PI3K/AKT Pathway under Diabetic Conditions. *Biomaterials* **2015**, *36*, 44−54.

(54) Wang, X. X.; Xie, L.; Wang, R. Z. Biological Fabrication of Nacreous Coating on Titanium Dental Implant. *Biomaterials* **2005**, *26*, 6229−6232.

(55) Jarcho, M.; Kay, J. F.; Gumaer, K. I.; Doremus, R. H.; Drobeck, H. P. Tissue, Cellular and Subcellular Events at A Bone-Ceramic Hydroxylapatite Interface. *J. Bioeng.* **1977**, *1*, 79−92.

(56) Biggs, M. J. P.; Richards, R. G.; Gadegaard, N.; McMurray, R. J.; Affrossman, S.; Wilkinson, C. D. W.; Oreffo, R. O. C.; Dalby, M. J. Interactions with Nanoscale Topography: Adhesion Quantification and Signal Transduction in Cells of Osteogenic and Multipotent Lineage. *J. Biomed. Mater. Res., Part A* **2009**, *91A*, 195−208.

(57) Palin, E.; Liu, H. N.; Webster, T. J. Mimicking The Nanofeatures of Bone Increases Bone-Forming Cell Adhesion and Proliferation. *Nanotechnology* **2005**, *16*, 1828−1835.

(58) Dalby, M. J.; McCloy, D.; Robertson, M.; Wilkinson, C. D. W.; Oreffo, R. O. C. Osteoprogenitor Response to Defined Topographies with Nanoscale Depths. *Biomaterials* **2006**, *27*, 1306−1315.